Research Square

Preprints are preliminary reports that have not undergone peer review.
They should not be considered conclusive, used to inform clinical practice,
or referenced by the media as validated information.

Satellite-observed greenness expansion across Antarctica

Min Chen

mchen392@wisc.edu

University of Wisconsin-Madison https://orcid.org/0000-0001-6311-7124

Hangkai You

hyou34@wisc.edu https://orcid.org/0000-0002-7678-947X

Taejin Park

NASA Ames Research Center

Christian Che-Castaldo

U.S. Geological Survey, Wisconsin Cooperative Wildlife Research Unit https://orcid.org/0000-0002-7670-2178

Dalei Hao

Pacific Northwest National Laboratory

Abhishek Chatterjee

Schmidt Sciences

Fa Li

The University of Texas at Austin https://orcid.org/0000-0002-0625-5587

Zhuosen Wang

Goddard Space Flight Center

Fujiang Ji

University of Wisconsin-Madison

Bilgecan Sen

Stony Brook University https://orcid.org/0000-0002-7393-1805

Yingjie Wang

Univ Toulouse, CNES/IRD/CNRS/INRAe

Matthew Lazzara

University of Wisconsin-Madison

Yanlan Liu

University of California Los Angeles https://orcid.org/0000-0001-5129-6284

Becky Ball

Arizona State University

Nicolas Lauret

Univ Toulouse

Eric Chavanon
Univ Toulouse

Article

Keywords:

Posted Date: November 9th, 2026

DOI: https://doi.org/10.21203/rs.3.rs-11568957/v1

License: This work is licensed under a Creative Commons Attribution 4.0 International License.
Read Full License

Additional Declarations: There is **NO** Competing Interest.

Title: Satellite-observed greenness expansion across Antarctica

Authors: Hangkai You[1]; Taejin Park[2,3]; Christian Che-Castaldo[4]; Dalei Hao[5]; Abhishek Chatterjee[6]; Fa Li[1,7]; Zhuosen Wang[8,9]; Fujiang Ji[1]; Bilgecan Sen[4]; Yingjie Wang[10]; Matthew A. Lazzara[11,12]; Yanlan Liu[13]; Becky Ball[14]; Nicolas Lauret[10]; Eric Chavanon[10]; Min Chen*[1].

Affiliations:

[1]Department of Forest and Wildlife Ecology, University of Wisconsin-Madison, Madison, Wisconsin, USA.

[2]NASA Ames Research Center, Moffett Field, California, USA.

[3]Bay Area Environmental Research Institute, Moffett Field, California, USA

[4]U.S. Geological Survey, Wisconsin Cooperative Wildlife Research Unit, Department of Forest and Wildlife Ecology, University of Wisconsin-Madison, Madison, Wisconsin, USA

[5]Atmospheric, Climate, & Earth Sciences Division, Pacific Northwest National Laboratory, USA

[6]Schmidt Sciences, New York, NY, USA

[7]Department of Earth and Planetary Sciences, Jackson School of Geosciences, The University of Texas at Austin, Austin, TX, USA

[8]Earth System Science Interdisciplinary Center, University of Maryland, College Park, College Park, Maryland, USA

[9]Terrestrial Information Systems Laboratory, NASA Goddard Space Flight Center, Greenbelt, Maryland, USA

[10]Univ Toulouse, CNES/IRD/CNRS/INRAe, CESBIO, Toulouse, France

[11]Antarctic Meteorological Research and Data Center, Space Science and Engineering Center, University of Wisconsin-Madison, Madison, Wisconsin, USA

[12]Department of Physical Sciences, School of Engineering, Science, and Mathematics, Madison Area Technical College, Madison, Wisconsin, USA

[13]Department of Geography, University of California, Los Angeles, California, USA

[14]School of Mathematical and Natural Sciences, Arizona State University, Glendale, Arizona, USA*Corresponding author. Email: min.chen@wisc.edu.

This draft manuscript is distributed solely for purposes of scientific peer review. Its content is deliberative and predecisional, so it must not be disclosed or released by reviewers. Because the manuscript has not yet been approved for publication by the U.S. Geological Survey (USGS), it does not represent any official USGS finding or policy.

Any use of trade, firm, or product names is for descriptive purposes only and does not imply endorsement by the U.S. Government.

Abstract: Polar ecosystems are reshaping rapidly in the 21st century, yet Antarctica's continent-wide terrestrial vegetation response remains unclear. Here, using 22 years (2002-2023) of daily MODIS products, we provide the first continent-wide, multi-decadal record of spectral greenness. The area of satellite product exhibiting greenness increased by more than 50%, from 7,356 to 11,219 km², and mean seasonal detection span lengthened from 22.6 to 32.4 days. Both trends were significant across all three major Antarctic regions. Water availability and ultraviolet radiation together account for 77% of modeled continental climate contributions, while temperature contributes less. Modeled regional contributions diverge sharply: water dominates in East Antarctica, ultraviolet-radiation on the Antarctic Peninsula, and ultraviolet-radiation and temperature jointly in West Antarctica. These results reveal shared spatial and seasonal greening across contrasting Antarctic changing environments.

Main:

The rapid environmental changes occurring across the globe are particularly evident at the poles, where ecological transformations are unfolding at an accelerated pace (*1*). While Arctic greening has been extensively studied and attributed primarily to rising temperatures (*2,3*), the patterns of greenness in Antarctica and their environmental associations remain poorly understood at the continental level (*4,5*). Antarctica's extremely cold and dry environment confines greenness to small ice-free habitats dominated by bryophytes, lichens, algae, cyanobacteria, and microbial communities (*6-8*). These ecosystems are particularly sensitive to shifts in environmental conditions (*8,9*). Both observational evidence and model projections suggest that Antarctica's terrestrial environment is undergoing shifts including ice retreat, soil moisture increase, and stratospheric ozone recovery (*10-14*), suggesting that greenness dynamics may also be changing (*4*). Accurately tracking these changes and understanding the associated environmental conditions is essential for assessing the continent's ecological response to global change (*4,15*).

Despite growing interest, continent-scale assessments of Antarctic greenness over multi-decadal timescales remain absent. Field-based ecological studies have begun to document site-scale vegetation change in recent years (*9*), while satellite-based efforts focus either on regional scales using Landsat or Sentinel-2 (*5*) or on time-invariant continental snapshots (*8*). Recent debate highlights the importance of consistent satellite coverage and field validation for interpreting Antarctic greening (*16-18*). No prior study has quantified continent-scale, multi-decadal changes in both the extent and seasonal duration of Antarctic greenness.

To address this gap, we compiled a 22-year dataset (2002-2023) of Antarctic greenness from Moderate Resolution Imaging Spectroradiometer (MODIS) observations (*19-23*). Throughout this study, 'greenness' refers to the MODIS-detected spectral signal at 500-m pixel scale, quantified by the Normalized Difference Vegetation Index (NDVI; see Methods). This metric identifies pixels carrying a detectable photosynthetic spectral signature; it does not directly map physical vegetation cover, which typically occupies sub-pixel area within Antarctic ice-free regions. MODIS's daily revisit and 500-m resolution enable continent-wide tracking of greenness dynamics across satellite observability windows (September-March) from 2002 to 2024. Cross-sensor comparisons with Sentinel-2, radiative-transfer simulations, and observation-condition diagnostics support the biological interpretation of the detected signals at continental scale (see Supplementary Materials).

To examine the environmental conditions associated with Antarctic greenness, we integrated the NDVI time series with complementary datasets (*24*). These include European Centre for Medium-Range Weather Forecasts (ECMWF) Reanalysis v5 (ERA5) climate variables (*25*), MODIS annual snow cover maps to delineate ice-free regions (*26*), and a digital elevation model to characterize terrain features (*27*). Together, these datasets enable continent-wide quantification of greenness extent, seasonal duration, decadal trends, and their associations with climatic conditions (Fig. 1).

Greenness Distribution in Antarctica

We define 'green area' as MODIS pixels with an annual maximum NDVI exceeding 0.2, computed as the pixel count multiplied by the 500-m pixel area (see Methods). This is a measure of the spatial extent over which a photosynthetic spectral signal is detectable, not of physical vegetation cover. The resulting distribution shows a strong coastal bias, with marked

concentration on the Antarctic Peninsula and scattered patches along the continental coastline (Fig. 1A). The Peninsula stands out, consistent with its milder maritime climate (average annual temperature ~-14 °C versus ~-46 °C inland; *25*), which enables longer periods of photosynthetic activity and more frequent detection of greenness. Coastal regions of East and West Antarctica also show scattered, often transient patches of greenness (Fig. 2, Fig. S1).

By contrast, the Antarctic interior remains largely devoid of greenness signal: permanent ice cover and extremely low temperatures prevent the exposure of substrates that could support photosynthetic activity (Fig. S1), and detections there are sparse and isolated. Ice-free regions such as the Transantarctic Mountains nevertheless host scattered patches of greenness (Fig. 2A). This pattern broadly aligns with the Sentinel-2 map of Walshaw et al. (*8*) but extends coverage to the 'pole hole' south of 82.8°S, beyond Sentinel-2's orbital reach.

Widespread but Uneven Expansion of Antarctic Greenness

Between September 2002 and March 2024, Antarctic green area showed substantial interannual variability but a significant overall expansion (Mann-Kendall $p < 0.05$, Sen's slope of 81.0 km² yr^{-1}; Fig. 1B). Total green area increased from 7,356 km² in 2002-2003 to 11,219 km² in 2023-2024, an increase of more than 50% between the first and last observability windows (green area increase signal is robust under multiple sensitivity tests, see Supplementary Materials). Regional trends are concordant: Antarctic Peninsula (Sen's slope of 15.1 km² yr^{-1}), West Antarctica (Sen's slope of 14.4 km² yr^{-1}), and East Antarctica (Sen's slope of 32.8 km² yr^{-1}) all show significant positive expansion (Mann-Kendall $p < 0.05$; Fig. 1B).

Expansion is concentrated in ice-free coastal regions, especially the Antarctic Peninsula, where milder maritime conditions support bryophytes, lichens, algae, cyanobacteria, and microbial communities (Fig. S1). Peak greenness reached 12,917 km² in the 2016-2017 observability window (Fig. 1B), coinciding with the strong 2016 El Niño-Southern Oscillation (ENSO) event that brought regional warming and increased moisture across the Southern Hemisphere (*28,29*); the long-term expansion persists after excluding this anomaly (Fig. S2).

Comparing the first five (2002-2006) and last five (2019-2023) observability windows reveals spatially uneven changes in green area, classified as stable (present in both periods), new (present only in the last five), or disappeared (present only in the first five) (Fig. 2A). New green area concentrates along the Antarctic Peninsula and the Transantarctic Mountains (Fig. 2B-C), while localized losses appear along parts of the East Antarctic coastline (Fig. 2D). Gains and losses are similar in magnitude, however, “disappeared” pixels do not necessarily indicate community loss: even when each period combines five observability windows, episodic greenness and variation in hydration and meltwater availability can affect detection. Despite this variability, both the aggregated extent and the annual series show a net increase in green area.

Extended Duration of Antarctic Greenness

In addition to spatial expansion, the seasonal duration of greenness has also lengthened across Antarctica. In this study, greenness duration is the number of days between the first and last NDVI > 0.2 detection within a pixel during the observability window (see Methods); this envelope metric bounds the active period rather than counting active days, and is well suited to taxa with continuous seasonal activity such as mosses and lichens while potentially overstating activity for ephemeral taxa that bloom briefly and repeatedly. At the continental scale, mean

greenness duration increased from 22.6 (±40.6) days in 2002 to 32.4 (±48.9) days in 2023 (Mann-Kendall $p < 0.001$, Sen's slope of 0.28 d yr^{-1}; Fig. 1C). Regional trends are concordant: East Antarctica (Sen's slope of 0.25 d yr^{-1}), West Antarctica (0.25 d yr^{-1}), and the Antarctic Peninsula (0.26 d yr^{-1}) all show significant duration extensions (Mann-Kendall $p < 0.05$; Fig. 1C).

Critically, this lengthening is not an artifact of the metric. An independent area-weighted duration measure based on a daily count of pixels exceeding NDVI > 0.2, which makes no use of first-and-last endpoints and is therefore insensitive to isolated tail detections, yields a similarly significant increase (Mann-Kendall $p < 0.001$; Fig. S24). The two metrics agree in direction and significance while differing in magnitude (Sen's slope 0.094 vs. 0.284 d yr^{-1}), consistent with their different definitions of greenness duration. The envelope-metric trend remains significant across the tested NDVI thresholds (Fig. S10), and both metrics remain significant under duration thresholds from 1 to 7 days (Fig. S12).

Although greenness duration and green area generally follow parallel upward trends, they are not always temporally synchronized. A notable divergence occurred during the 2016-2017 austral summer, which coincided with a strong 2016 ENSO event and an abrupt decline in sea ice (*29,30*). During this period, green area expanded markedly, yet mean greenness duration decreased to 20.8 (±32.6) days, which was 34% lower than the preceding year. This divergence likely reflects rapid colonization of newly exposed ice-free surfaces by ephemeral organisms such as snow algae and biocrust microalgae, responding to increased meltwater availability (Fig. S1, S4). Despite this ENSO-driven reduction, the long-term increase in greenness duration remains when years with large deviations are excluded (Fig. S5). By contrast, established bryophyte and lichen communities sustain detectable photosynthetic activity from weeks to months (*7,9,31-35*), supporting longer durations where present.

Environmental Associations of Antarctic Greenness Trends

To resolve the environmental conditions associated with Antarctic greenness trends, we employed a random forest (RF) model to predict green area fraction, defined as the proportion of MODIS pixels with NDVI > 0.2 within each 0.1° grid cell, and partitioned the modeled trend among variables using Shapley value decomposition (see Methods). By design, this is an attribution of explained signal among co-varying environmental variables, which we interpret in concert with independent ecophysiological evidence and with a complementary detrending analysis described below; its strength comes from the convergence of these lines. Each environmental variable was decomposed into spatial (geographic heterogeneity), temporal (long-term and interannual variability), and residual (local deviations) components, all of which served as RF inputs (see Methods). The RF achieved robust performance across both continental and regional models under 5-fold spatiotemporal cross-validation (Fig. S6, S7, see Supplementary Materials).

Random forest permutation importance, which quantifies how sensitive model predictions are to each input variable, shows that the predicted green area fraction depends much more on spatial differences in environmental conditions across Antarctica than on interannual variability at any single location (Data S1). This pattern reflects the strong heterogeneity of Antarctic climate: contrasts between ice-free coast and high-elevation interior, or maritime Peninsula and cold-desert East, are typically larger than interannual variability at any given location. Predictions in East Antarctica are most sensitive to ice-free area ratio, consistent with a habitat-limited regime

where exposed substrate is a key constraint. On the Antarctic Peninsula, predictions depend more on climatic variables (UV radiation, precipitation), suggesting a transition from a habitat-limited to a more climate-responsive greenness regime as conditions become milder (*36, 37*). Because permutation importance reflects predictive sensitivity rather than causal contribution, we attribute the temporal greenness trend to specific climate variables separately, using Shapley value analysis.

Shapley value analysis apportions the modeled greenness trend among variables according to each variable's average marginal contribution across all variable combinations, with shares summing to the model-explained portion of the trend (see Methods). At the continental scale, water availability (volumetric soil water 35%, precipitation 21%) and ultraviolet radiation (21%) jointly account for ~77% of the modeled trend, with smaller shares from temperature (8%) and other variables; all eight Shapley values are positive (Fig. 3). The regional contrast is sharper and, as developed below, tracks the known ecophysiology of each region. In East Antarctica, where habitat availability is the binding spatial constraint, water variables alone explain ~69% of the modeled trend (volumetric soil water 53%, precipitation 16%), matching a water-limited cold-desert regime. On the Antarctic Peninsula, where habitat is no longer limiting, UV radiation leads the attribution (46%), potentially consistent with reduced photodamage stress under stratospheric ozone recovery. West Antarctica shows a transitional pattern, with UV (39%) and temperature (29%) jointly accounting for ~68% of the modeled regional trend.

Ecological Context and Implications

The regional Shapley pattern is consistent with an interpretable ecological gradient (*4, 7*). In East Antarctica, the cold-desert environment likely makes liquid water the primary biological constraint (*4, 7, 35*). Antarctic bryophytes, lichens, and microalgae are largely poikilohydric (*38*): their photosynthetic activity depends directly on external moisture, so increases in volumetric soil water and precipitation can translate to longer photosynthetically active periods and stronger detected NDVI signal (*15*). Although stratospheric ozone recovery is most pronounced over the East Antarctic plateau, extreme cold, desiccation, and sparse ice-free substrate prevent organisms from benefiting much from reduced UV stress there; UV is not the limiting factor in this region. The Antarctic Peninsula occupies a different regime: milder maritime conditions and abundant moisture (*37*) release water and temperature limits, leaving UV stress as a larger relative bottleneck. Reduced UV diminishes photoinhibition and the energetic cost of photoprotective pigments (*39*), allowing more chlorophyll-driven photosynthesis and a stronger detected greenness signal. The climate-explained fraction of the modeled greenness trend declines from East (~97%) to the Peninsula (~72%). Additional processes, including glacial retreat (*10*) and sea-ice variability (*30*), may also shape greenness dynamics in maritime Antarctica. Together, these regional contributions correspond to a model-based estimate of ~54.5% ±2.1% of the observed continental greenness trend associated with climate trends.

The come-and-go pattern of Antarctic greenness across years (Figs. S1, S4) likely reflects the stochastic ecology of these extreme environments. Many Antarctic photosynthetic organisms reproduce by spores, soredia, or fragments dispersed by strong polar winds (*40*), and to a lesser extent by birds and other wildlife visiting summer breeding sites (*41*). Most dispersed propagules likely fail to establish: they may land on unsuitable substrate, experience rapid desiccation, or be carried away before colonization can occur. Where local conditions transiently provide liquid

water and stable substrate, however, occasional successful establishment events generate detectable greenness signal that may persist for years or fade as conditions change. In addition to colonization dynamics, NDVI in lichens and biocrusts varies substantially with hydration state (*38*): a dry year may suppress signal at otherwise stable sites, while a wet year may activate dormant communities. Ephemeral snow algae similarly bloom transiently when meltwater becomes available (*42*), generating short-lived NDVI signals tied to specific melt events. These mechanisms (stochastic dispersal, conditional establishment, hydration cycling, and ephemeral blooms) together likely explain the spatial-temporal turnover observed at decadal scales.

The more than 50% expansion of detected spectral greenness signal should not directly be interpreted as an equivalent increase in vegetation cover or biomass. NDVI at MODIS scale aggregates signals from multiple taxa with differing chlorophyll content, hydration state, and physiological responses (*4*), so a stronger signal can reflect activation of existing communities, expansion of new colonies, or some combination at sub-pixel scales. Antarctic photosynthetic organisms typically occupy surfaces three to four orders of magnitude smaller than a single MODIS pixel: Direct UAV surveys at three Windmill Islands sites cover valid mapped areas equivalent to only 2.32 to 4.96% of a single MODIS pixel; detected moss within these surveyed areas occupies less than 1% of a co-located MODIS pixel (Fig. S8). This scale gap renders direct field-to-pixel regression structurally inappropriate for validating pixel-level greenness products, because a ground measurement and a MODIS pixel sample fundamentally different fractions of the same surface. Continental-scale validation must therefore operate at intermediate scales: cross-sensor comparison with Sentinel-2 (10 m), which is small enough to resolve the moss-rock mosaic yet co-located with MODIS pixels, combined with radiative-transfer simulations that establish the pixel-scale detectability of sub-pixel vegetation. Both validation paths confirm that MODIS-detected greenness corresponds to a biologically meaningful spectral signal at the continental scale (see Supplementary Materials). Our results therefore document a coarse-scale ecological response detectable from continental-scale satellite observation, with species-level dynamics within pixels remaining a target for dedicated UAV and ground-based campaigns.

Looking ahead, ongoing intensification of the Antarctic water cycle and continued stratospheric ozone recovery suggest potentially sustained pressure for further greenness expansion across the continent. The biological response is unlikely to be linear, however: where water and UV constraints are relaxed in the Peninsula, succession, biological inertia, and emerging interactions among taxa may modulate the trajectory in ways that satellite signal alone cannot resolve. Continental-scale satellite observation (MODIS, Sentinel-2, Landsat) combined with high-resolution UAV surveys at index sites and in-situ ecological transects offers the framework needed to track how Antarctic terrestrial systems respond to coupled water-cycle and ozone-recovery dynamics. Emerging hyperspectral missions such as NASA's PACE further enable taxonomic discrimination of photosynthetic organism groups through pigment signatures (*43*), opening a path toward observing not only how much greenness changes but which communities are responding.

Materials and Methods

Normalized Difference Vegetation Index Data

In this study, "greenness" refers to the spectral signature associated with photosynthetic or photosynthetically capable surface features, quantified using the Normalized Difference Vegetation Index (NDVI). In the Antarctic context, greenness reflects contributions from photosynthetic life-bearing substrates such as mosses, lichens, algae, microbial mats, etc (*8*).

To derive the daily NDVI for the Antarctic region, we used the Moderate Resolution Imaging Spectroradiometer (MODIS) C6.1 Nadir Bidirectional Reflectance Distribution Function (BRDF)-Adjusted Reflectance (NBAR) Product MCD43A4 (*22*). This 500-m product applies a BRDF kernel inversion using a 16-day rolling window, in which observations closer to the target day receive higher weights. As a result, the retrieved reflectance represents the surface conditions most characteristic of that specific day while minimizing variability caused by changing illumination and viewing geometry. Extensive evaluations have shown that the BRDF-corrected MCD43 products provide a stable and physically consistent reflectance basis for long-term greenness analyses in high-latitude environments (*44,45*). In particular, Wang et al. demonstrated that the MCD43 algorithm effectively captures rapid day-to-day surface variation and that full and magnitude inversions achieve similarly high accuracy (*46*). This evidence underpins the widespread use of BRDF-corrected MCD43 data in vegetation remote-sensing studies. The NDVI was computed using the near-infrared (NIR) and red (RED) reflectance bands according to the formula:

$$NDVI=(NIR-RED)/(NIR+RED)$$

We defined the Antarctic region as the area south of 60 °S latitude, with the continental boundary extracted for analysis (see Geographic Data section below) to focus on dynamics of greenness within the terrestrial regions of Antarctica.

To ensure consistent observation conditions, we selected 2002 as the starting year of the analysis, as both Terra and Aqua satellites were fully operational by this time. This allows the merged dataset to maintain a uniform observation frequency, reducing potential biases associated with differing satellite overpass times. Considering the polar night and the passive optical nature of MODIS sensors, we defined a specific observation window, from September 23 to March 21 of the following year, as the growing season. This window spans the austral spring and summer, when solar illumination permits optical monitoring across Antarctica.

MODIS MCD43A4 data were accessed through Google Earth Engine (GEE) Data Catalog and processed to generate daily NDVI products based on band calculation during each observability window (*47*). The observability window does not assume continuous biological growth across Antarctica, which clearly varies by region and taxon. Instead, it marks the period during which MODIS has sufficient illumination and surface exposure to detect spectral signals of greenness. We then use these detectable signals to assess long-term changes in terrestrial greenness across the continent.

Greenness Distribution Mapping

Traditional field-based monitoring presents significant challenges due to Antarctica's extreme and remote conditions, making large-scale and repeatable data collection logistically difficult and often temporally and spatially fragmented (*7*). This limitation is particularly critical given the short, sporadic, and highly variable nature of greenness events in Antarctica, which demand frequent observations to accurately detect and characterize vegetation activity. While satellite-based remote sensing provides a powerful alternative for long-term, spatially extensive monitoring (*35*), many commonly used high-resolution sensors such as Sentinel-2 and Landsat,

despite their spatial detail (10-30 m), offer limited and temporally inconsistent coverage and may miss key greenness events. Given the short greenness duration in Antarctica, frequent observations are essential in tracking key phenological cycles accurately (*5,8*). These gaps can lead to an underestimation of the distribution and duration of greenness activity. In contrast, the MODIS sensors on Terra and Aqua provide daily global observations at 500 m resolution, enabling high-frequency tracking of vegetation indices. MODIS's daily revisit enhances both temporal detection and spatial coverage of transient greenness events across Antarctica, including regions south of 82.8° S that are beyond the reach of many sensors.

To map greenness across Antarctica, we conducted a comprehensive literature review and analyzed spectral measurements specific to the region. Based on this review, we applied a NDVI threshold of 0.2 to each pixel for the NDVI products we generated before (see "Normalized Difference Vegetation Index Data" section), and any pixel with at least one day exceeding this threshold during a given year was classified as exhibiting greenness and contributed to that year's "green area" (area of greenness detected by satellite spectral signal) estimate (*5,8,16-20*). The 0.20 threshold lies well above the reflectance characteristics of snow, ice, and most bare rock surfaces in Antarctica, ensuring that MODIS-classified 'green' pixels contain a non-trivial fraction of vegetated cover or vegetation-like spectral properties at the 500-m scale. Because Antarctic vegetation typically occupies surfaces far smaller than a 500-m MODIS pixel, the resulting mapped "green area" should not be interpreted as the physical area of vegetated ground. Instead, it represents a MODIS-detectable spectral greenness signal—an integrated sub-pixel response that indicates where strong greenness occurs within the mixed surface footprint. Accordingly, all area values reported in km² refer to the spatial extent of MODIS-detectable greenness signals, rather than true vegetation cover.

To represent the overall spatial distribution of greenness across Antarctica during the study period, we created a frequency of greenness map (Fig. 1A), which records the number of years greenness was observed at each pixel. For each year, if a pixel's NDVI exceeded the threshold of 0.2 at any point during the observability window, it was counted as a greenness occurrence for that year. By summing these annual occurrences across all years, we obtained a spatial greenness distribution map indicating how many years each pixel exhibited greenness.

To quantify long-term trends in Antarctic greenness, we calculated the total green area for each observability window (2002-2023), both at the continental scale and each biogeographic region (see "Geographic Data" section). We assessed trends in green area using the Mann-Kendall (MK) test and report their p-values to determine significance. We also fitted linear regression models and showed the slope values as an estimate of trend magnitude over time (Fig. 1B). Because the observability window spans two calendar years, we used the first calendar year of each observability window (such as 2002 for the 2002-2003 season) as the year input for both MK tests and linear regression models.

To evaluate the robustness of the NDVI threshold of 0.2, we repeated the green area trend analysis using alternative thresholds. Green area trends remained positive across all tested NDVI thresholds and were significant at thresholds of 0.15–0.30 (Fig. S9). Greenness duration trends remained significant across the tested NDVI thresholds (Fig. S10).

To further investigate the drivers of green area distribution and trends in green area expansion, we used a random forest (RF) model (see "Machine Learning Modeling and Analysis" section). Given the 500-meter resolution of MODIS data, we calculated the green area fraction within each 0.1-degree grid cell, defined as the ratio of green area (i.e., area of pixels with NDVI larger than 0.2) to the total land area within the grid cell, to align with other input variables used for the RF model.

Antarctica Continent Greenness Duration Mapping

Daily NDVI data derived from the MODIS MCD43A4 was used to study greenness duration across the Antarctic continent for each observability window. Although MCD43A4 is generated through a 16-day moving window for BRDF inversion, it is not a 16-day composite. The algorithm applies strong temporal weighting, giving greatest influence on observations closest to the target date, and yields a BRDF-corrected reflectance that is most representative of surface conditions on that day. This approach reduces angular noise, enforces strict quality control, and has been widely adopted for daily-scale phenology and long-term NDVI analyses in polar and cryosphere environments. The use of a moving window can smooth short-lived greenness pulses and introduce timing uncertainty on the order of several days.

We first applied a mask to exclude pixels with a maximum NDVI below 0.2 within a given observability window, thereby removing areas without large enough greenness signal from observations. For each remaining pixel, greenness duration was calculated as the number of days between the first and last dates when NDVI exceeded 0.2, representing the seasonal span of satellite detectable greenness signal(*48*).

To quantify long-term trend in greenness duration, we calculated the area-weighted mean greenness duration for each observability window at both the continental scale and each biogeographic region (see "Geographic Data" section). Temporal trends of the annual area weighted greenness duration were assessed using MK test, and their slopes were calculated based on linear regressions. To test the sensitivity of our results to the NDVI threshold, we repeated the analysis using different thresholds (see section "Sensitivity to NDVI and Duration-Day Thresholds"). Same as what we did in green area trend calculation, we used the first calendar year of each observability window as the year input for both MK tests and linear regression models.

Sensitivity to NDVI and Duration-Day Thresholds

To evaluate the robustness of our results to threshold choices, we conducted sensitivity analyses for both the green-area trend and the mean greenness-duration trend across two threshold types: the NDVI threshold used to classify a pixel as "green", and the minimum number of qualifying days within each observability window. For each analysis, we applied a range of threshold values and assessed whether the resulting trends remained significant.

For the green area trend, we varied the NDVI threshold from 0.1 to 0.3 in increments of 0.05. At each threshold, we recalculated the total green area across the Antarctic continent for each observability window. We then applied the MK test to evaluate the statistical significance of the temporal trend and fitted a linear regression model to estimate its slope over the study period, based on the green area results derived from each NDVI threshold (Fig. S9).

For the greenness duration trend, we varied the NDVI threshold from 0.1 to 0.3 in increments of 0.1. At each threshold, we recalculated the area-weighted mean greenness duration across the Antarctic continent, defined as the number of days between the first and last dates when NDVI exceeded the threshold for each pixel in each observability window. As with the green area trend, we applied the MK test to assess the statistical significance of the greenness duration trend under different NDVI thresholds and used linear regression to estimate its slope over time (Fig. S10).

For the duration-day threshold, we required NDVI > 0.2 to be exceeded on at least T days within each observability window, with T varying from 1 to 14 days. At each T, we recomputed the annual continental green-area total and the area-weighted mean greenness duration using both the first-and-last-day method and the daily-count method (see "Antarctica Continent

Greenness Duration Mapping"), then applied the MK test and computed Sen's slope on the resulting time series.

Base Geographic Data

Several base geographic data recording the continent's land mask and subregions were used in this study. The Antarctica continent land mask used in this study was obtained from Hijmans et al. from University of California, Berkeley (*49*). For biogeographic regional analysis, we utilized the biogeographic subregion map derived from the Basins Antarctica dataset provided by the NASA Making Earth System Data Records for Use in Research Environments (MEaSUREs) Antarctic Boundaries for IPY 2007-2009 from Satellite Radar, Version 2 (*50*). In this study, the Antarctic continent includes East Antarctica, West Antarctica, the Antarctic Peninsula, and surrounding offshore islands. We conducted regional analyses for three major biogeographic regions: the Antarctic Peninsula, West Antarctica, and East Antarctica. While surrounding islands were included in the hexagonal aggregation to provide a comprehensive view of continent-wide greenness patterns, we excluded them from RF modeling and biogeographic region-specific green area and greenness duration trend analyses due to their small size and sparse distribution.

Environmental Data

To predict the spatial distribution and temporal dynamics of Antarctic green area occurrence, and to investigate their potential environmental drivers, we assembled a suite of environmental variables as predictors for the RF models (see "Machine Learning Modeling and Analysis" section). These variables represent key climatic and topographic conditions that influence green area occurrence across the continent.

Topographic data for this study were obtained from the Antarctic 1-km Digital Elevation Model (DEM), which integrates satellite altimetry measurements from the European Remote Sensing Satellite-1 (ERS-1) Radar Altimeter and the Ice, Cloud, and land Elevation Satellite (ICESat) Geosciences Laser Altimeter System (GLAS) (*27*). The resulting DEM provides comprehensive coverage at 1-km resolution across the Antarctic continent. Using ArcMap 10.8.2, we derived topographic variables aspect from the DEM. To ensure alignment with other input predictors in RF models, aspect was aggregated to a 0.1° resolution using area weighted mean method. Since the aspect data are time invariant, we directly used them as the input predictor into the RF models without decomposition.

Ice-free area data were obtained from the MODIS Terra Snow Cover Daily Global 500m product (MOD10A1.061) via GEE (*26*). This product provides daily estimates of snow cover as percentage values ranging from 0 to 100%, representing the area proportion of each pixel covered by snow. Only observations with quality flags labeled as "Best" or "Good" were retained. For each observability window (2002-2023), we calculated the minimum snow cover and identified ice-free regions where snow cover remained below 30%. To facilitate integration with other input predictors in RF models, we upscaled the MODIS snow cover data to a 0.1° resolution, which computed the area fraction of the MODIS pixels with ice-free regions within each grid cell instead of using a binary classification. This approach produced a continuous representation of snow-free extent across Antarctica, rather than a binary classification, improving the robustness of environment-green area interaction assessments.

Meteorological data for this study were derived from the European Centre for Medium-Range Weather Forecasts (ECMWF) Reanalysis v5 (ERA5) post-processed daily statistics on single levels, a global reanalysis dataset provided by the ECMWF, spanning from 1940 to the present (*25*), which provides spatially complete and internally consistent climate fields widely

used in Antarctic studies (*51*). ERA5 has been shown to reproduce the observed temperature and wind variability at Antarctic stations with acceptable bias during the modern satellite era (*52*). ERA5 radiation fields, including UV-related components, show small errors at monthly-annual scales in high-latitude evaluations, making them suitable for the seasonal to half-yearly averages used in this study (*53*).To ensure consistency across variables and compatibility with other datasets, we resampled all variables to a common 0.1° spatial resolution using a nearest-neighbor aggregation method. For each climate variable, we calculated the mean value over each observability window. These variables included 2-m mean air temperature, UV radiation, solar radiation, volumetric soil water, runoff, 10-m wind speed, precipitation, and vapor pressure deficit, all of which play critical roles in Antarctic green area occurrence responses by influencing energy balance, water availability, and atmospheric moisture conditions (*4*). To enhance interpretability in the RF models, each climate variable was further decomposed into spatial, temporal, and residual components (see "Machine Learning Modeling and Analysis" section).

MODIS-Sentinel-2 Cross-Sensors Validation

To evaluate uncertainty in the MODIS green area and link MODIS detections to sub-pixel green area cover, we compared MODIS-derived green area with 10 m green area derived by Sentinel-2. For each observability window, we identified all land pixels whose maximum NDVI from the MODIS MCD43A4 product (500 m) exceeded one of three thresholds (0.10, 0.15, or 0.20). For each such pixel, we extracted all Sentinel-2 Level-2A surface-reflectance observations falling within the MODIS footprint and assembled a growing-season image collection restricted to scenes with <10% cloud cover and mean solar-zenith angles <70°. Clouds were removed using the Sentinel-2 Scene Classification Layer, and NDVI was computed from the red (B4) and near-infrared (B8) bands. Each Sentinel-2 pixel was assigned its maximum NDVI in the corresponding growing season and labelled "green" when this value exceeded a certain threshold (0.10, 0.15, or 0.20). This procedure was repeated across all MODIS-Sentinel-2 threshold combinations.

From all MODIS pixels with valid Sentinel-2 coverage and at least one Sentinel-2 green pixel, we retained a fixed sample of up to 1,000 MODIS-Sentinel-2 pairs per growing season (sampling done independently across seasons, so locations could recur). For each retained pair, we recorded the MODIS maximum NDVI, the number of Sentinel-2 green pixels, and the total number of valid 10 m pixels within the footprint. These data were used to estimate the mean sub-pixel green-coverage fraction associated with each MODIS green area threshold class.

Cross-Study Green Area Alignment

To enable a like-for-like comparison of the area between MODIS-derived detections and the estimates reported by Walshaw et al. (*8*), we reproduced the spatial filtering used in their analysis and applied it to our green area map. The mask consisted of three elements: consistent permanent rock map; a DEM filter retaining only areas with elevation under 500 meters; and a latitudinal constraint excluding all regions south of 83°S (the practical limit of Sentinel-2 acquisition).

We first reprojected the Permanent Rock shapefile into the native projection of the MODIS raster grid and rasterized the mask at 500 m resolution. The MODIS pixels with DEM (see "Environmental Data" Section) below 500 meters were filtered. We computed center latitudes of pixels and retained only those north of 83°S. We then applied this composite mask to our green area map and calculated the green area trend.

Sub-pixel scale-mismatch between satellite and field observations

Antarctic vegetation typically occupies surfaces several orders of magnitude smaller than a MODIS pixel: individual moss and lichen patches can range from centimeters to a few meters across, while field quadrats and UAV imagery sample square-meter to tens-of-meter footprints. A single 500 m MODIS pixel therefore integrates a heterogeneous mix of bare rock, snow, ice, and small vegetation patches, and any quantitative match between a MODIS-detected greenness signal and a single field or UAV measurement is necessarily mediated by the unresolved sub-pixel mosaic (Fig. S8F). To illustrate the magnitude of this scale gap, we compared UAV-derived green-area estimates and field-quadrat vegetation cover (*54*) with co-located MCD43A4 NDVI at three Windmill Islands sites (Fig. S8) At all three sites the MODIS signal is consistent with the presence of vegetation but quantitatively reflects a much larger ice and rock background, so direct one-to-one cross-validation between continental MODIS products and small-footprint ground observations is not appropriate. The cross-sensor MODIS-Sentinel-2 comparison and the DART-based detectability simulations described above provide more scale-consistent validation paths.

Cloud and Land Observation Frequency Analysis

To assess whether long-term changes in observation conditions could artefactually amplify MODIS greenness trends, we quantified seasonal cloudiness and land-observation fraction over Antarctica using MODIS atmosphere products from both Terra and Aqua. We used the monthly Level-3 MODIS cloud products MOD08_M3 (Terra) and MYD08_M3 (Aqua) Collection 6.1 (*55*) and extracted two variables: the mean cloud fraction (Cloud_Fraction_Mean_Mean) and the daytime land fraction within the cloud-top pressure retrieval area (Land_Fraction_Day_FMean).

All analyses were restricted to the Southern Hemisphere high latitudes (south of 60°S). For each monthly image in MOD08_M3 and MYD08_M3, we computed an area-weighted mean cloud fraction and land fraction over this region. We then aggregated these monthly statistics into observability window means consistent with our greenness analysis. To test for trends in these time series, we applied the Mann-Kendall test separately to the cloud-fraction and land-fraction series from MOD08_M3 and MYD08_M3.

Trend Robustness to Outlier Years

To test whether MODIS greenness trends were unduly influenced by anomalous years, we identified statistical outliers using ±2σ and ±3σ thresholds, where σ denotes the standard deviation of each metric across observability windows. No years exceeded the ±3σ threshold, which therefore served as the unfiltered baseline. The ±2σ filter flagged a small number of unusually high or low years, and these were removed in separate sensitivity experiments.

For each σ-filter configuration, we rebuilt the corresponding time series and recalculated trends in green area and mean greenness duration. Linear trend slopes were estimated using ordinary least squares, and trend significance was assessed using the non-parametric MK test, yielding independent estimates of trend magnitude and statistical significance under each outlier-removal scenario.

Radiative Transfer Simulations

To mechanistically evaluate the sensitivity and robustness of MODIS-equivalent NDVI to sub-pixel vegetation abundance, substrate composition, terrain structure, and viewing geometry, we implemented a coordinated suite of forward simulations using the Discrete Anisotropic Radiative Transfer (DART) model (https://dart.omp.eu), which is one of the most accurate and complete 3D radiative transfer models (*56,57*) and can simulate the radiative budget and remote

sensing signals of natural and urban landscapes, from visible to thermal infrared. All simulations used the exact MODIS red and NIR band specifications embedded directly into the forward model (Band 1: 645 ± 25 nm; Band 2: 858 ± 17.5 nm), allowing DART to integrate reflectance across the prescribed spectral windows and return physically consistent MODIS-equivalent NDVI without any post-hoc convolution (see "Spectral Libraries Generation").

Using the synthetic land-cover and DEM surfaces (see "Synthetic Landscapes Construction" section), we generated several sets of simulations designed to isolate the primary physical controls on NDVI in Antarctic landscapes. The first set of simulations explored how NDVI responds to controlled changes in vegetation abundance within mixed vegetation-rock-snow mosaics. These experiments spanned the full range of plausible sub-pixel vegetation cover, from sparse lichen or algae patches to more continuous biological crusts, while holding DEM, illumination and viewing geometry fixed. This allowed us to quantify how much vegetation is required to produce a detectable NDVI signal in a MODIS-sized footprint and how this detection threshold varies with background substrate.

To quantify how snow and ice suppress the detectability of green area in MODIS-equivalent NDVI, we designed a second set of forward simulations in which green area was held at trace abundances and snow cover was incrementally increased until green area became undetectable. All experiments used a flat, rock-dominated synthetic landscape with fixed illumination and viewing geometry (solar zenith, sensor zenith, solar azimuth, and view azimuth held constant) to ensure that the results isolate spectral-mixing effects rather than BRDF artefacts or topographic shading. For each snow-cover increment, we introduced a small vegetation fraction into the remaining snow-free area and then gradually increased this vegetation fraction until the simulated band-integrated MODIS NDVI surpassed the threshold (NDVI > 0.2). If no vegetation fraction within a physically realistic range could generate NDVI above this threshold, the snow fraction was deemed to exceed the detectability limit. By repeating the procedure across a sequence of snow fractions, we derived the theoretical minimum vegetation fractions required for detectability under each snow-background scenario, as well as the snow-cover values beyond which NDVI-based green area detection becomes impossible.

The third set of simulations assessed NDVI variability driven solely by terrain geometry and bidirectional reflectance effects. Using the synthetic DEMs (see "Synthetic Landscapes Construction" section) spanning combinations of slope magnitude (mild, moderate, steep) and surface roughness (smooth, undulating, high-relief), we quantified how topographic shading, anisotropic reflectance, and slope-aspect alignment influence MODIS-equivalent NDVI independent of vegetation structure. To isolate terrain and angular effects from compositional variability, all experiments used a fixed land cover (Rock 50% and Algae 50%), allowing directional artefacts to be evaluated under controlled spectral conditions. Each DEM was paired with this land-cover map and subjected to systematic sweeps of solar zenith angle, view-zenith angle, and relative azimuth differences. To fully characterize directional sensitivity, we additionally conducted azimuth-rotation experiments in which the illumination azimuth, sensor azimuth, or the terrain itself was rotated in 30° increments through 0-330°. These simulations explicitly test whether NDVI is disproportionately influenced by slope orientation, self-shadowing, or BRDF effects under Antarctic illumination regimes.

Synthetic Landscapes Construction

For each DART run, we constructed a series of synthetic landscapes which is composed of two parts: synthetic land cover and synthetic DEM. To represent Antarctic surface heterogeneity at sub-meter scale, we generated synthetic 500 m × 500 m land-cover maps at 1 m resolution that prescribe the spatial distribution of snow, algae, moss, lichen, and exposed rock for all DART

simulations. Each class was assigned a distinct spatial pattern to fit better with Antarctic ground-cover organization (Fig. S18). Snow and algae were created as clustered, spatially coherent patches by applying smoothed random fields, reflecting the tendency of snowfields and algal communities to occur in contiguous microtopographic basins rather than as isolated pixels. In contrast, moss and lichen were placed as sparse, fine-scale patches stochastically distributed across rock surfaces, mirroring their natural occurrence in discontinuous cushions or crusts on desert pavements. Rock served as the background substrate for all unassigned pixels. For each experiment, we controlled surface composition explicitly by specifying target fractional cover for all green area and snow classes; these fractions were converted to exact pixel counts, and classes were allocated sequentially (clustered classes first, followed by sparse classes) to ensure that the realized composition matched the prescribed totals. To capture the influence of local relief and slope on surface reflectance, we also constructed a suite of synthetic 500 m × 500 m DEMs at 1 m resolution for use in DART. Each DEM was generated from first principles to isolate specific topographic configurations while maintaining realistic Antarctic micro-terrain structure (Fig. S19). We first prescribed a base elevation field and imposed a unidirectional planar slope of controlled magnitude (0°, moderate, and steep). To introduce natural small-scale variability, we added Gaussian-smoothed stochastic noise, tuned via amplitude and smoothing kernels to mimic gentle undulations and micro-relief without imposing unrealistic roughness. Depending on the experiment, we further varied the overall relief amplitude (10-30 m) and slope fraction to create DEMs with mild, intermediate, and strong relief, producing a total of six distinct terrain scenarios. All DEMs were then rescaled to a fixed elevation range to ensure comparability across simulations. Each surface was exported as a triangulated mesh (OBJ format) matched exactly to the land-cover grid, enabling DART to model the combined effects of topography, shadowing, and bidirectional reflectance geometry.

Spectral Libraries Generation

Surface optical properties were assigned using measured spectral libraries. Spectra for rock, moss, lichen, and green algae were obtained from Walshaw et al. (*8*), and snow and blue-ice reflectance spectra were taken from the cryospheric dataset (*58*). All spectra were resampled to DART's internal wavelength grid and assigned to the synthetic land-cover classes on a per-pixel basis. This combination of Antarctic-specific vegetation spectra and physically based snow-ice optics ensures that the simulated surface reflectance is mechanistically realistic and representative of true polar conditions.

Machine Learning Modeling and Analysis

To investigate how environmental conditions are associated with Antarctic green area distribution and its temporal dynamics, we constructed a two-step modeling pipeline. In the first step, we used random forest (RF) models (*59*) to predict the green-area fraction at 0.1° resolution girds from environmental variables across Antarctica, and within each biogeographic region; in the second step, per-0.1°-grid predictions are aggregated, to yield annual green-area time series. Climate-variable attribution targets these aggregated time series, so it reflects the composite behavior of pixel-scale prediction together with spatial aggregation rather than any single internal component. The first step RF was trained using only spatial, temporal, and residual components of the environmental variables (see "Decomposition Methods"). Importantly, no explicit time variable (e.g., year or date) was included as a predictor, so the RF was not fit to a temporal index but instead learned associations between MODIS-detected green area and contemporaneous environmental conditions. In this analysis, the RF serves strictly as a predictive mapping rather than a causal model; attribution of the temporal greenness trend to specific

climate variables is performed separately by Shapley value analysis on the full pipeline (see "Shapley Value Attribution Method").

To evaluate the first step predictive performance while avoiding overfitting, we used a 5-fold spatiotemporal cross-validation scheme. The dataset was divided into five folds that each contained a representative mix of different regions and years. Because the RF does not receive time as an input, this design prevents the model from implicitly learning long-term trends and ensures that model skill reflects robust environmental-green area relationships rather than temporal autocorrelation. In each fold, 80% of the data were used for training and 20% for testing. Model performance was quantified using the mean coefficient of determination (R^2) and root-mean-squared error (RMSE) across the five test folds. In addition, we trained five independent RF models (one in each fold) and used their mean and standard deviation of model performance and permutation importance to evaluate stability across folds. The same procedure was applied to both continental and regional RF models. The 5-fold spatiotemporal cross-validation confirms the stability of the first step mapping across independent subsets of space and time, which is essential for the Shapley attribution analysis at the second step: it ensures that the attribution results are not sensitive to fold partitioning or training-data composition.

To characterize how environmental factors relate to MODIS-detected spectral greenness signal area, we applied two diagnostic analyses on top of the pipeline. Permutation importance is applied to the first step alone and quantifies the predictive sensitivity of the RF model to each input variable. Shapley value attribution operates on the full two-step pipeline and allocates the predicted continental, and regional, greenness trend among the climate variables. To maintain consistency with the validation framework, both diagnostics were computed as the mean across the five cross-validation RF models. Analyses were performed at both continental and biogeographic regional scales to assess spatial variability in these statistical relationships.

Decomposition Methods

To disentangle the effects of environmental factors on Antarctic green area distribution and green area trend, we followed previous work to decompose the input data into three components, which are temporal, spatial, and residual components (*60,61*). Let $x_{i,t}$ be an environmental variable at cell i and year t, then the temporal component is an average across sites for each year t, $x_{time} = \sum_{i=1}^{N} x_{i,t} \div N$; the spatial component is an average across years for each cell i, $x_{space} = \sum_{t=1}^{T} x_{i,t} \div T$; and the residual component is the remaining spatio-temporal variation in $x_{i,t}$, $x_{residual} = x - x_{time} - x_{space}$. The temporal component captures shared interannual variability, reflecting year-to-year changes common across the continent. The spatial component reflected geographic heterogeneity, distinguishing regions with differing environmental conditions. The residual component captures local fluctuations not explained by broad temporal or spatial patterns.

Permutation Importance Analysis

To quantify how sensitive the random forest predictions are to each input variable, we performed permutation feature importance analysis at both continental and biogeographic regional scales using the scikit-learn package in Python, within the 5-fold spatiotemporal cross-validation framework described above. The procedure shuffles one variable at a time across all samples and measures the resulting decline in model R^2; a larger decline indicates greater predictive sensitivity to that variable. We emphasize that permutation importance reflects how strongly the RF model relies on each variable to predict greenness signal at any given time and place, and is therefore a measure of predictive sensitivity, not of causal contribution to the

temporal trend. The full set of permutation importance values for the continental and the three regional random forest models is provided in Data S1.

Detrending of Climatic Variables

To support the Shapley value attribution analysis (see "Shapley Value Attribution Method"), we generated counterfactual environmental fields in which the long-term linear trend of selected variables was removed while interannual variability was preserved. These detrended fields serve as the no-trend inputs of the Shapley value function: comparing the random forest's predicted green-area trajectory under original versus detrended inputs isolates the contribution of each variable's long-term trend to the predicted green-area trend. For reference, the long-term trends (Sen's slope and MK p-value) of each environmental variable at continental and biogeographic-regional scales are tabulated in Data S4. The spatial distribution of each environmental variable across the three biogeographic regions is shown in Fig. S13, and the pixel-wise long-term trend of each variable, computed only over pixels exhibiting a greenness spectral signal, is shown in Fig. S14.

We performed detrending separately at every 0.1° grid cell. For each environmental variable, we fitted an ordinary least-squares linear regression of annual values on calendar year, then subtracted the fitted trend line from the time series. To preserve the variable's typical magnitude at each cell, we added back the long-term mean of the original time series at that cell. The resulting series is centered at the cell's long-term mean and contains the original year-to-year variability with the long-term linear trend removed. Anchoring at the long-term mean rather than at an endpoint year keeps the detrended values close to the bulk of the training data, so that the random forest is queried within its calibrated input range when the detrended fields are used as Shapley counterfactuals. Example modeled continental green-area trajectories under representative detrending counterfactuals are shown in Fig. S22.

Detrending was applied only to the temporal and residual components of each variable (see "Decomposition Methods"); the spatial component is time-invariant by construction and was left unchanged (*62*). When the Shapley analysis required detrending a group of variables jointly, the procedure above was applied to each member of the group while all variables outside the group retained their observed trajectories.

As a sanity check on the Shapley results, we additionally re-applied the five cross-validated random forest models to each detrended counterfactual and tested the Mann-Kendall significance of the resulting continental and regional predicted green-area trends, following the combinatorial procedure of our earlier analysis. The pattern of significance loss across variable combinations is consistent with the Shapley shares reported in the main text (Fig. S23).

Shapley Value Attribution Method

To partition the modeled long-term green-area trend among individual climate variables in a way that respects their correlated and non-linear interactions, we used Shapley value attribution from cooperative game theory (*63*) as a data-driven decomposition of the modeled trend rather than a causal-inference framework. The Shapley value provides the unique allocation that is symmetric across players, assigns zero to non-contributing players, is linear in the underlying value function, and satisfies the efficiency property whereby the assigned shares sum exactly to the total trend produced by the model. These properties avoid the order-dependence and arbitrary baseline choices that arise when more than two variables jointly co-vary.

The Shapley value treats attribution as a cooperative game in which N climate variables jointly produce an outcome (the modeled green-area trend) and asks how much each variable

contributes on average across all possible coalitions $S \subseteq N$. We defined the value function $v(S)$ as follows. For each subset S, we kept the variables in S at their observed trajectories while replacing all variables in $N \setminus S$ with their detrended counterfactuals (see "Detrending of Climatic Variables"); time-invariant predictors retained their observed values throughout. We then applied the first step random forest to obtain per-pixel green-area fraction predictions for every year and aggregated them in the second step to produce a continental (or regional) annual green-area time series. The Sen's slope of this time series defines $v(S)$, the modeled green-area trend that emerges when only the variables in S retain their long-term trends. By construction, $v(\emptyset)$ approximates zero (all variable trends removed) and $v(\mathrm{N})$ equals the full modeled trend (all variables retained). Climate-trend attribution therefore operates on the full two-step pipeline rather than on any single internal step.

The Shapley value for variable i is:

$$\varphi_i = \sum_{S \subseteq N \setminus \{i\}} \frac{|S|!\,(N - |S| - 1)!}{N!} [v(S \cup \{i\}) - v(S)]$$

the weighted average marginal contribution of variable i across all coalitions that do not contain it. By the efficiency property, $\sum_{i \in N} \varphi_i = v(N) - v(\emptyset)$, so the Shapley shares partition the modeled total trend exactly.

With eight climate variables, the value function was evaluated on all $2^8 = 256$ coalitions: a single no-detrend reference run, an all-variables-detrended run, and every intermediate combination. For each coalition we generated the detrended inputs at each 0.1° grid cell, applied each of the five cross-validation random forest models from the first step, averaged the predictions to obtain the green-area time series, and computed the Sen's slope of that series as $v(S)$. The same procedure was used at the continental scale and at each biogeographic region, with each region using its own region-specific random forest.

To quantify uncertainty in the Shapley shares, we computed φ_i separately for each of the five cross-validation random forest models. Reported shares are the mean across the five folds, and the standard deviation provides a fold-level estimate of attribution uncertainty. This bounds the contribution of training-data composition to the attribution result.

References and Notes

1. I. H. Myers-Smith, J. T. Kerby, G. K. Phoenix, J. W. Bjerke, H. E. Epstein, et al., Complexity revealed in the greening of the Arctic. Nat. Clim. Chang. 10, 106–117 (2020). doi:10.1038/s41558-019-0688-1
2. R. B. Myneni, C. D. Keeling, C. J. Tucker, G. Asrar, R. R. Nemani, Increased plant growth in the northern high latitudes from 1981 to 1991. Nature 386, 698–702 (1997). doi:10.1038/386698a0
3. L. T. Berner, R. Massey, P. Jantz, B. C. Forbes, M. Macias-Fauria, I. Myers-Smith, T. Kumpula, G. Gauthier, L. Andreu-Hayles, B. V. Gaglioti, P. Burns, P. Zetterberg, R. D'Arrigo, S. J. Goetz, Summer warming explains widespread but not uniform greening in the Arctic tundra biome. Nat. Commun. 11, 4621 (2020). doi:10.1038/s41467-020-18479-5
4. P. Convey, L. S. Peck, Antarctic environmental change and biological responses. Sci. Adv. 5, eaaz0888 (2019). doi:10.1126/sciadv.aaz0888
5. T. P. Roland, O. T. Bartlett, D. J. Charman, K. Anderson, D. A. Hodgson, M. J. Amesbury, I. Maclean, P. T. Fretwell, A. Fleming, Sustained greening of the Antarctic Peninsula observed from satellites. Nat. Geosci. 17, 1121–1126 (2024). doi:10.1038/s41561-024-01564-5
6. J. Singh, R. P. Singh, R. Khare, Influence of climate change on Antarctic flora. Polar Sci. 18, 94–101 (2018). doi:10.1016/j.polar.2018.05.006
7. C. Colesie, C. V. Walshaw, L. G. Sancho, M. P. Davey, A. Gray, Antarctica's vegetation in a changing climate. WIREs Clim. Change 14, e810 (2023). doi:10.1002/wcc.810
8. C. V. Walshaw, A. Gray, P. T. Fretwell, P. Convey, M. P. Davey, J. S. Johnson, C. Colesie, A satellite-derived baseline of photosynthetic life across Antarctica. Nat. Geosci. 17, 755–762 (2024). doi:10.1038/s41561-024-01492-4
9. N. Cannone, F. Malfasi, S. E. Favero-Longo, P. Convey, M. Guglielmin, Acceleration of climate warming and plant dynamics in Antarctica. Curr. Biol. 32, 1599–1606.e2 (2022). doi:10.1016/j.cub.2022.01.074
10. J. R. Lee, B. Raymond, T. J. Bracegirdle, I. Chadès, R. A. Fuller, J. D. Shaw, A. Terauds, Climate change drives expansion of Antarctic ice-free habitat. Nature 547, 49–54 (2017). doi:10.1038/nature22996
11. M. Siegert, A. Atkinson, A. Banwell, M. Brandon, P. Convey, B. Davies, R. Downie, T. Edwards, B. Hubbard, G. Marshall, J. Rogelj, J. Rumble, J. Stroeve, D. Vaughan, The Antarctic Peninsula under a 1.5°C global warming scenario. Front. Environ. Sci. 7, 102 (2019). doi:10.3389/fenvs.2019.00102
12. X. Fang, J. A. Pyle, M. P. Chipperfield, J. S. Daniel, S. Park, R. G. Prinn, Challenges for the recovery of the ozone layer. Nat. Geosci. 12, 592–596 (2019). doi:10.1038/s41561-019-0422-7
13. A. D. Kennedy, Antarctic terrestrial ecosystem response to global environmental change. Annu. Rev. Ecol. Syst. 26, 683–704 (1995). doi:10.1146/annurev.es.26.110195.003343
14. H. A. Fricker, B. K. Galton-Fenzi, C. C. Walker, B. I. D. Freer, L. Padman, R. DeConto, Antarctica in 2025: Drivers of deep uncertainty in projected ice loss. Science 387, 601–609 (2025). doi:10.1126/science.adt9619

15. N. Cannone, M. Guglielmin, F. Malfasi, H.-W. Hubberten, D. Wagner, Rapid soil and vegetation changes at regional scale in continental Antarctica. Geoderma 394, 115017 (2021). doi:10.1016/j.geoderma.2021.115017

16. C. Colesie, A. M. Gray, C. V. Walshaw, S. Bokhorst, J. T. Kerby, S. Jawak, L. G. Sancho, P. Convey, Is Antarctica greening?. Glob. Chang. Biol. 31, e70294 (2025). doi:10.1111/gcb.70294

17. Bokhorst, S., Huisman, S.N., de Jonge, I.K. et al. Antarctic greening is constrained by biology and requires field validation. Nat. Geosci. (2026). https://doi.org/10.1038/s41561-026-02076-0

18. Roland, T.P., Bartlett, O.T., Charman, D.J. et al. Reply to: Antarctic greening is constrained by biology and requires field validation. Nat. Geosci. (2026). https://doi.org/10.1038/s41561-026-02080-4

19. Y. Zeng, D. Hao, A. Huete, B. Dechant, J. Berry, J. M. Chen, J. Joiner, C. Frankenberg, B. Bond-Lamberty, Y. Ryu, J. Xiao, G. R. Asrar, M. Chen, Optical vegetation indices for monitoring terrestrial ecosystems globally. Nat. Rev. Earth Environ. 3, 477–493 (2022). doi:10.1038/s43017-022-00298-5

20. V. V. Salomonson, X. Xiong, Introduction to MODIS and an overview of associated activities, in Earth Science Satellite Remote Sensing, J. J. Qu, W. Gao, M. Kafatos, R. E. Murphy, V. V. Salomonson, Eds. (Springer, 2006), 12–32. doi:10.1007/978-3-540-37293-6_2

21. C. B. Schaaf, F. Gao, A. H. Strahler, W. Lucht, X. Li, T. Tsang, N. C. Strugnell, X. Zhang, Y. Jin, J.-P. Muller, P. Lewis, M. Barnsley, P. Hobson, M. Disney, G. Roberts, M. Dunderdale, C. Doll, R. P. d'Entremont, B. Hu, S. Liang, J. L. Privette, D. Roy, First operational BRDF, albedo nadir reflectance products from MODIS. Remote Sens. Environ. 83, 135–148 (2002). doi:10.1016/S0034-4257(02)00091-3

22. C. Schaaf, Z. Wang, MODIS/Terra+Aqua BRDF/Albedo Nadir BRDF-Adjusted Reflectance Daily L3 Global 500m V061 [dataset]. NASA Land Processes Distributed Active Archive Center (2021). doi:10.5067/MODIS/MCD43A4.061

23. P. S. A. Beck, C. Atzberger, K. A. Høgda, B. Johansen, A. K. Skidmore, Improved monitoring of vegetation dynamics at very high latitudes: A new method using MODIS NDVI. Remote Sens. Environ. 100, 321–334 (2006). doi:10.1016/j.rse.2005.10.021

24. R. Schofield, E. D. Rudolph, Factors influencing the distribution of Antarctic terrestrial plants. Antarct. J. U.S. 4, 112–113 (1969).

25. Copernicus Climate Change Service (C3S), ERA5 hourly data on single levels from 1940 to present [dataset]. Copernicus Climate Data Store (2018). doi:10.24381/cds.adbb2d47

26. D. K. Hall, G. A. Riggs, MODIS/Terra Snow Cover Daily L3 Global 500m SIN Grid, Version 61 [dataset]. NASA National Snow and Ice Data Center DAAC (2021). doi:10.5067/MODIS/MOD10A1.061

27. J. L. Bamber, J. L. Gomez-Dans, J. A. Griggs, Antarctic 1 km Digital Elevation Model (DEM) from Combined ERS-1 Radar and ICESat Laser Satellite Altimetry, Version 1 [dataset]. NASA National Snow and Ice Data Center DAAC (2009). doi:10.5067/H0FQ1KL9NEKM

28. A. Santoso, M. J. McPhaden, W. Cai, The defining characteristics of ENSO extremes and the strong 2015/2016 El Niño. Rev. Geophys. 55, 1079–1129 (2017). doi:10.1002/2017RG000560

29. J. A. Bodart, R. J. Bingham, The impact of the extreme 2015–2016 El Niño on the mass balance of the Antarctic Ice Sheet. Geophys. Res. Lett. 46, 13862–13871 (2019). doi:10.1029/2019GL084466

30. L. Zhang, T. L. Delworth, X. Yang, F. Zeng, F. Lu, Y. Morioka, M. Bushuk, The relative role of the subsurface Southern Ocean in driving negative Antarctic sea ice extent anomalies in 2016–2021. Commun. Earth Environ. 3, 302 (2022). doi:10.1038/s43247-022-00624-1

31. M. J. Amesbury, T. P. Roland, J. Royles, D. A. Hodgson, P. Convey, H. Griffiths, D. J. Charman, Widespread biological response to rapid warming on the Antarctic Peninsula. Curr. Biol. 27, 1616–1622.e2 (2017). doi:10.1016/j.cub.2017.04.034

32. M. Guglielmin, M. Dalle Fratte, N. Cannone, Permafrost warming and vegetation changes in continental Antarctica. Environ. Res. Lett. 9, 045001 (2014). doi:10.1088/1748-9326/9/4/045001

33. R. D. Seppelt, R. Türk, T. G. A. Green, G. Moser, S. Pannewitz, L. G. Sancho, B. Schroeter, Lichen and moss communities of Botany Bay, Granite Harbour, Ross Sea, Antarctica. Antarct. Sci. 22, 691–702 (2010). doi:10.1017/S0954102010000568

34. S. N. Power, V. A. Thomas, M. R. Salvatore, J. E. Barrett, Habitat suitability of biocrust communities in a cold desert ecosystem. Ecol. Evol. 14, e11649 (2024). doi:10.1002/ece3.11649

35. D. M. Bergstrom, S. L. Chown, Life at the front: history, ecology and change on southern ocean islands. Trends Ecol. Evol. 14, 472–477 (1999). doi:10.1016/S0169-5347(99)01688-2

36. T. A. Day, C. T. Ruhland, C. W. Grobe, F. Xiong, Growth and reproduction of Antarctic vascular plants in response to warming and UV radiation reductions in the field. Oecologia 119, 24–35 (1999). doi:10.1007/s004420050757

37. R. E. Longton, Plant and invertebrate ecology. Philos. Trans. R. Soc. Lond. B 252, 213–235 (1967). doi:10.1098/rstb.1967.0014

38. J. D. Wasley, S. A. Robinson, C. E. Lovelock, M. Popp, Some like it wet, biological characteristics underpinning tolerance of extreme water stress events in Antarctic bryophytes. Funct. Plant Biol. 33, 443–455 (2006). doi:10.1071/FP05306

39. S. A. Robinson, D. J. Erickson III, Not just about sunburn, the ozone hole's profound effect on climate has significant implications for Southern Hemisphere ecosystems. Glob. Chang. Biol. 21, 515–527 (2015). doi:10.1111/gcb.12739

40. W. A. Marshall, Aerial dispersal of lichen soredia in the maritime Antarctic. New Phytol. 134, 523–530 (1996). doi:10.1111/j.1469-8137.1996.tb04370.x

41. Y. Frenot, S. L. Chown, J. Whinam, P. M. Selkirk, P. Convey, M. Skotnicki, D. M. Bergstrom, Biological invasions in the Antarctic: Extent, impacts and implications. Biol. Rev. 80, 45–72 (2005). doi:10.1017/S1464793104006542

42. A. Gray, M. Krolikowski, P. Fretwell, P. Convey, L. S. Peck, M. Mendelova, A. G. Smith, M. P. Davey, Remote sensing reveals Antarctic green snow algae as important terrestrial carbon sink. Nat. Commun. 11, 2527 (2020). doi:10.1038/s41467-020-16018-w

43. S. Caplan, K. F. Huemmrich, Unveiling PACE OCI's hyperspectral terrestrial data products. Remote Sens. Lett. 16, 422–433 (2025). doi:10.1080/2150704X.2025.2470905

44. J. C. Stroeve, J. E. Box, Z. Wang, C. Schaaf, A. Barrett, Re-evaluation of MODIS MCD43 Greenland albedo accuracy and trends. Remote Sens. Environ. 138, 199–214 (2013). doi:10.1016/j.rse.2013.07.023

45. Z. Wang, C. B. Schaaf, M. J. Chopping, A. H. Strahler, J. Wang, M. O. Román, A. V. Rocha, C. E. Woodcock, Y. Shuai, Evaluation of Moderate-resolution Imaging Spectroradiometer (MODIS) snow albedo product (MCD43A) over tundra. Remote Sens. Environ. 117, 264–280 (2012). doi:10.1016/j.rse.2011.10.002

46. Z. Wang, C. B. Schaaf, Q. Sun, Y. Shuai, M. O. Román, Capturing rapid land surface dynamics with Collection V006 MODIS BRDF/NBAR/Albedo (MCD43) products. Remote Sens. Environ. 207, 50–64 (2018). doi:10.1016/j.rse.2018.02.001

47. N. Gorelick, M. Hancher, M. Dixon, S. Ilyushchenko, D. Thau, R. Moore, Google Earth Engine: Planetary-scale geospatial analysis for everyone. Remote Sens. Environ. 202, 18–27 (2017). doi:10.1016/j.rse.2017.06.031

48. Y. Zeng, B. D. Wardlow, D. Xiang, S. Hu, D. Li, A review of vegetation phenological metrics extraction using time-series, multispectral satellite data. Remote Sens. Environ. 237, 111511 (2020). doi:10.1016/j.rse.2019.111511

49. R. J. Hijmans, Boundary, Antarctica, 2015 [Global Administrative Areas version 2.8]. Museum of Vertebrate Zoology, University of California, Berkeley, and International Rice Research Institute (2015). https://purl.stanford.edu/yk702xd7587

50. J. Mouginot, B. Scheuchl, E. Rignot, MEaSUREs Antarctic Boundaries for IPY 2007-2009 from Satellite Radar, Version 2 [dataset]. NASA National Snow and Ice Data Center DAAC (2017). doi:10.5067/AXE4121732AD

51. S. Stammerjohn, T. A. Scambos, S. Adusumilli, S. Barreira, G. H. Bernhard, D. Bozkurt, S. M. Bushinsky, K. R. Clem, S. Colwell, L. Coy, J. De Laat, M. D. du Plessis, R. L. Fogt, A. Foppert, H. A. Fricker, A. S. Gardner, S. T. Gille, T. Gorte, B. Johnson, E. Keenan, D. Kennett, L. M. Keller, N. A. Kramarova, K. Lakkala, M. A. Lazzara, J. T. M. Lenaerts, J. L. Lieser, Z. Li, H. Liu, C. S. Long, M. MacFerrin, M. L. Maclennan, R. A. Massom, D. Mikolajczyk, L. Montgomery, T. L. Mote, E. R. Nash, P. A. Newman, I. Petropavlovskikh, M. Pitts, P. Reid, S. R. Rintoul, M. L. Santee, E. H. Shadwick, A. Silvano, S. Stierle, S. Strahan, A. J. Sutton, S. Swart, V. Tamsitt, B. Tilbrook, L. Wang, N. L. Williams, X. Yuan, Antarctica and the Southern Ocean [in "State of the Climate in 2020"]. Bull. Am. Meteorol. Soc. 102, S317–S356 (2021). doi:10.1175/BAMS-D-21-0081.1

52. D. H. Bromwich, A. Ensign, S.-H. Wang, X. Zou, Major artifacts in ERA5 2-m air temperature trends over Antarctica prior to and during the modern satellite era. Geophys. Res. Lett. 51, e2024GL111907 (2024). doi:10.1029/2024GL111907

53. B. Babar, R. Graversen, T. Boström, Solar radiation estimation at high latitudes: Assessment of the CMSAF databases, ASR and ERA5. Sol. Energy 182, 397–411 (2019). doi:10.1016/j.solener.2019.02.058

54. D. King, S. Robinson, J. Wasley, Windmill Islands Long Term Vegetation Monitoring, Version 1 [dataset]. Australian Antarctic Data Centre (2020). doi:10.26179/5eaf718e45748

55. S. Platnick, et al., MODIS Atmosphere L3 Monthly Product (MOD08_M3) [dataset]. NASA MODIS Adaptive Processing System, Goddard Space Flight Center (2015). doi:10.5067/MODIS/MOD08_M3.061

56. J.-P. Gastellu-Etchegorry, V. Demarez, V. Pinel, F. Zagolski, Modeling radiative transfer in heterogeneous 3-D vegetation canopies. Remote Sens. Environ. 58, 131–156 (1996). doi:10.1016/0034-4257(95)00253-7

57. Y. Wang, T. Yin, N. Lauret, E. Chavanon, J.-P. Gastellu-Etchegorry, DART-Lux: An unbiased and rapid Monte Carlo radiative transfer method for simulating remote sensing images. Remote Sens. Environ. 274, 112973 (2022). doi:10.1016/j.rse.2022.112973

58. R. Casacchia, R. Salvatori, A. Cagnati, M. Valt, S. Ghergo, Field reflectance of snow/ice covers at Terra Nova Bay, Antarctica. Int. J. Remote Sens. 23, 4653–4667 (2002). doi:10.1080/01431160110113863

59. L. Breiman, Random forests. Mach. Learn. 45, 5–32 (2001). doi:10.1023/A:1010933404324

60. U. Bradter, A. Johnston, W. M. Hochachka, A. Soultan, J. E. Brommer, E. Gaget, J. A. Kålås, A. Lehikoinen, Å. Lindström, S. Piirainen, D. Pavón-Jordán, T. Pärt, I. J. Øien, B. K. Sandercock, et al., Decomposing the spatial and temporal effects of climate on bird populations in northern European mountains. Glob. Chang. Biol. 28, 6209–6227 (2022). doi:10.1111/gcb.16355

61. C. S. Oedekoven, S. T. Buckland, M. L. Mackenzie, R. King, K. O. Evans, L. R. Burger, Attributing changes in the distribution of species abundance to weather variables using the example of British breeding birds. Methods Ecol. Evol. 8, 1690–1702 (2017). doi:10.1111/2041-210X.12811

62. F. Li, Q. Zhu, W. J. Riley, L. Zhao, L. Xu, K. Yuan, M. Chen, H. Wu, Z. Gui, J. Gong, J. T. Randerson, AttentionFire_v1.0: Interpretable machine learning fire model for burned-area predictions over tropics. Geosci. Model Dev. 16, 869–884 (2023). doi:10.5194/gmd-16-869-2023

63. L. S. Shapley, A value for n-person games, in Contributions to the Theory of Games, Volume II (Annals of Mathematics Studies 28), H. W. Kuhn, A. W. Tucker, Eds. (Princeton Univ. Press, 1953), 307–317.

Acknowledgments:

We thank Dr. Thomas Kurosu from Jet Propulsion Laboratory, California Institute of Technology for his valuable insights during the early stages of this work.

Funding:

Support for this research was provided by the Office of the Vice Chancellor for Research and Graduate Education, University of Wisconsin-Madison, with funding from the Wisconsin Alumni Research Foundation.

Author contributions: Conceptualization: HY, MC; Methodology: HY, CC, FL, BS, TP, YW, MC; Visualization: HY, FJ; Funding acquisition: MC; Project administration: MC; Supervision: TP, CC, MC; Writing – original draft: HY; Writing – review & editing: All authors.

Competing interests: Authors declare that they have no competing interests.

Data, code, and materials availability: All data used in this study are all open access and are listed in supplementary materials. The code developed for this project can be found at GitHub repository (https://github.com/UW-GCRL/Antarctic_Greening_and_Its_Drivers).

Supplementary Materials

Supplementary Text

Figs. S1 to S24

References (*42–61*)

Data S1 to S4

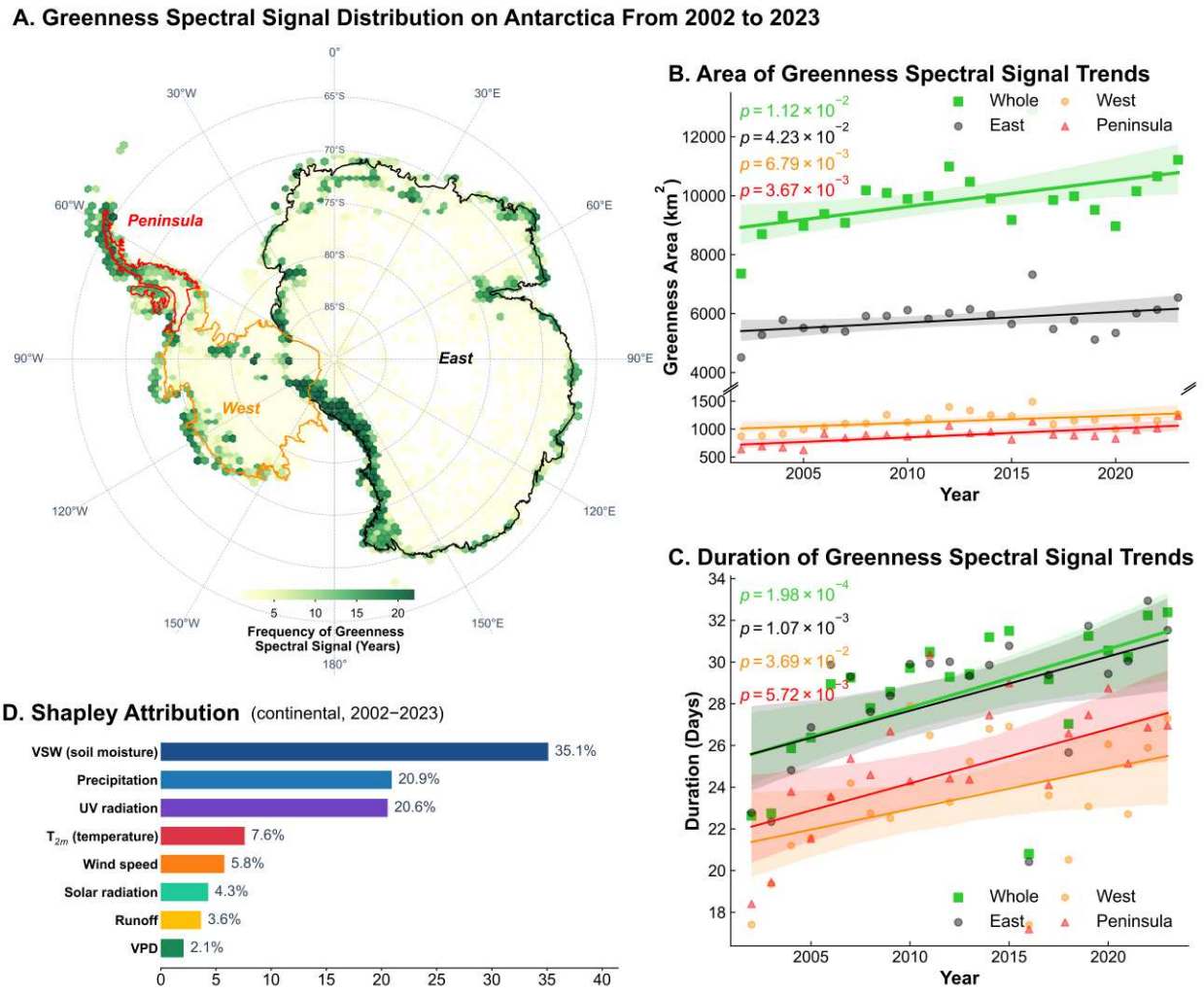


Fig. 1. Antarctic greenness expansion and Shapley attribution to climate variables. Frequency of MODIS-detected greenness across Antarctica during 2002–2023. The map is hexagonally binned; each hexagon summarizes the number of years in which at least one pixel within the hexagon exhibited a maximum NDVI > 0.2 during the observability window. Hexagonal counts describe detection frequency and do not represent actual green area. Biogeographic regions are outlined: Antarctic Peninsula (red), West Antarctica (yellow), and East Antarctica (black). (B) Annual greenness area (km²) for the whole continent (green), East Antarctica (gray), West Antarctica (orange), and the Antarctic Peninsula (red), 2002–2023. Solid lines are linear-regression fits; Mann-Kendall p-values are annotated for each region. The y-axis is broken to accommodate the magnitude difference between the continental aggregate and the regional series. (C) Area-weighted mean greenness duration (days) for the same regions and period, with linear-regression fits (solid lines), Mann-Kendall p-values, and 95% confidence intervals of the fit (shaded bands). (D) Continental Shapley attribution of the 2002–2023 greenness-area trend among the eight climate variables: volumetric soil water (VSW), precipitation, UV radiation, 2-m temperature (T2 m), wind speed, solar radiation, runoff, and vapor pressure deficit (VPD).

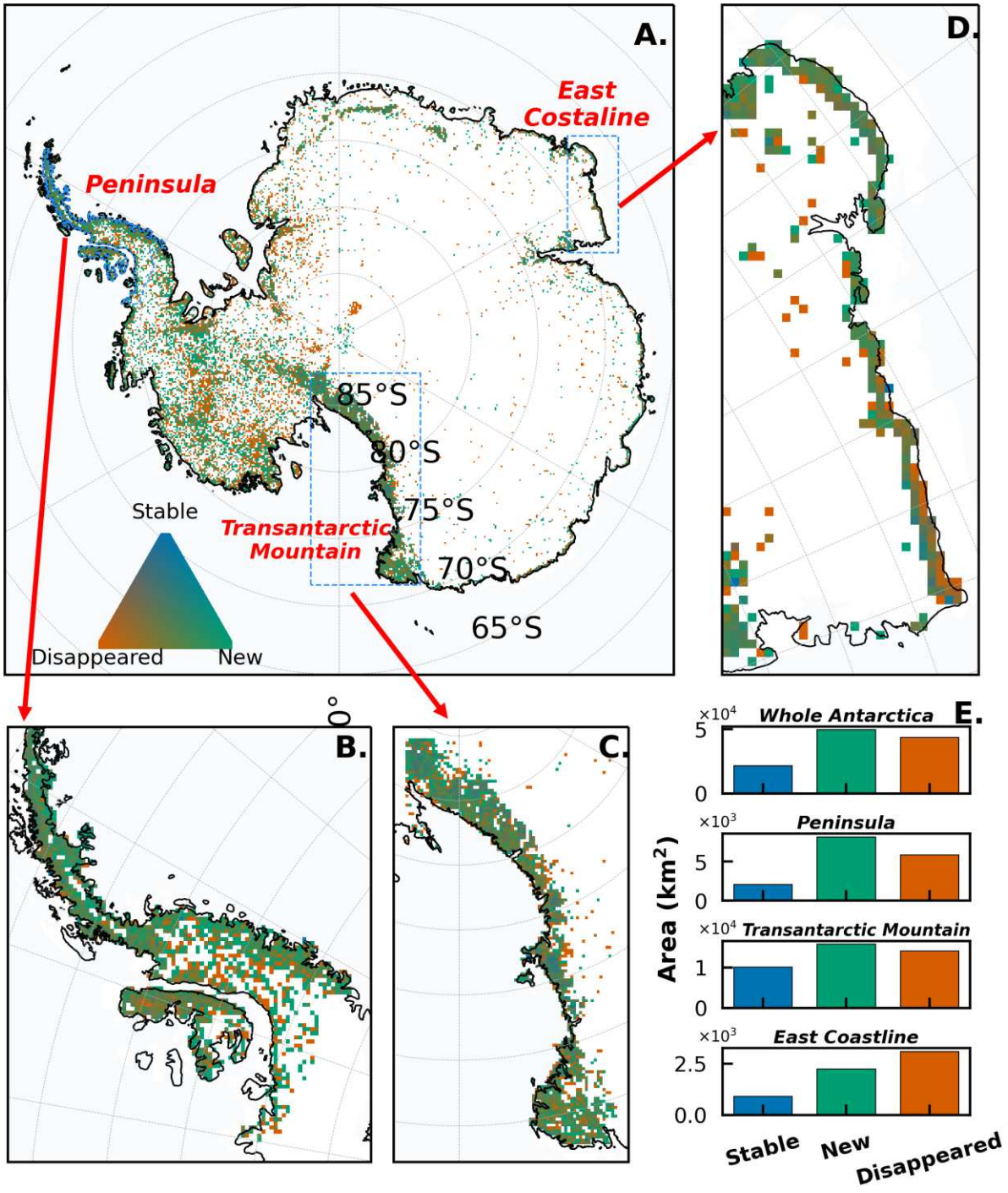


Fig. 2. Spatial shifts in Antarctic green area. A. The spatial pattern of green area dynamics between the first five years' observability window (2002-2006) and the last five years' observability windows (2019-2023) of the study period. Each displayed grid cell represents a 40×40 Moderate Resolution Imaging Spectroradiometer (MODIS) pixel aggregation block and shows the percentage composition of green area pixels categories within that block, rather than actual green area. A ternary color scheme is used to indicate green area pixels' status at each grid cell: bluer indicates grid cell which tends to have more stable green area (present both in the first

five years' observability windows and last five years' observability windows); increasing orange indicates a higher proportion of disappeared green area (present in the first five years' observability windows but absent in the last five years' observability windows); and increasing green indicates a higher proportion of new green area (absent in the first five years' observability windows but present in the last five years' observability windows). (B-D) Zoomed-in views of green area dynamics in three key regions: (B) Antarctic Peninsula, (C) transantarctic mountains, and (D) East Antarctic coastline. (E) Total area of stable, new, and disappeared green area for the regions shown in Panels A-D. Sensitivity of area estimates to NDVI threshold selection is provided in Fig. S3.

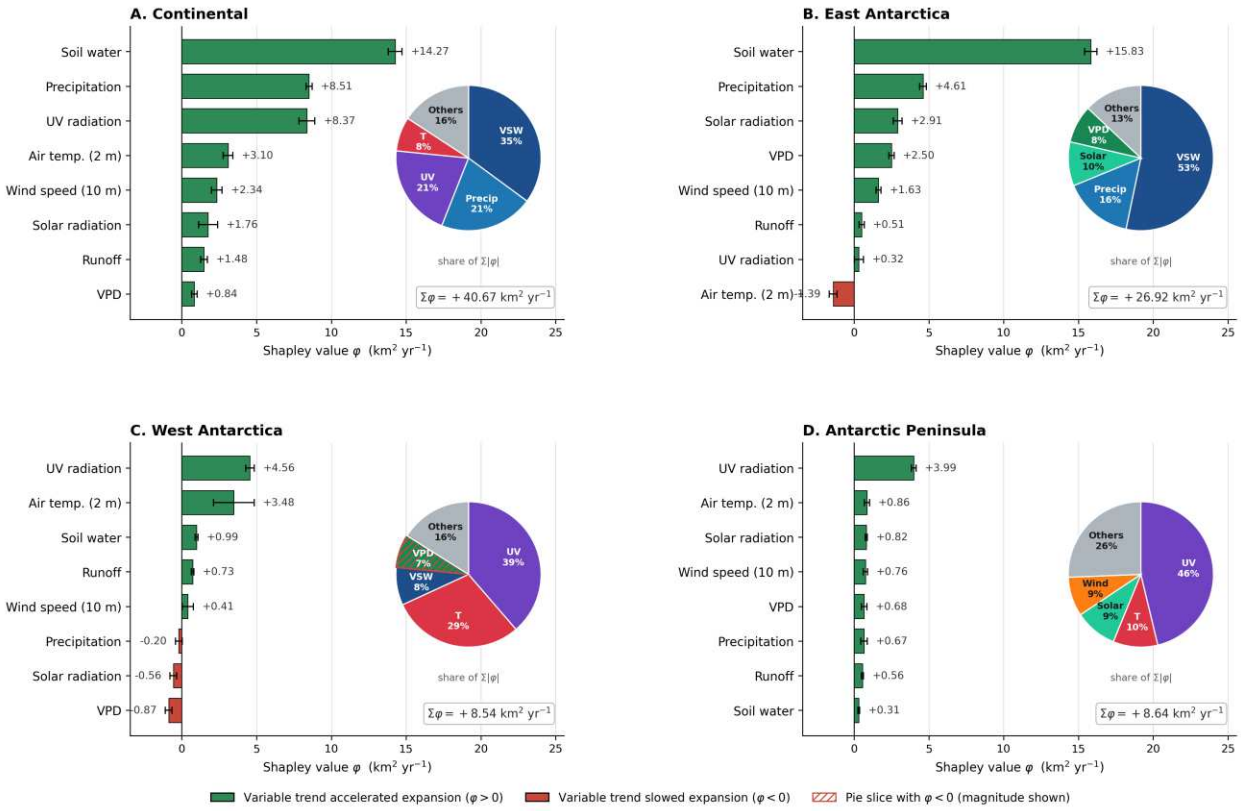


Fig. 3. Shapley attribution of models derived climate-driven green area expansion across Antarctic. Subpanels show the per-variable Shapley values (φ, km² yr^{-1}) for the eight potential climate drivers of green area expansion in (A) Antarctica continent, (B) East Antarctica, (C) West Antarctica, and (D) the Antarctic Peninsula, respectively. Green bars ($\varphi > 0$) indicate variables whose 2002–2023 trend, on net, accelerated green area expansion; red bars ($\varphi < 0$) indicate variables whose trend slowed it. Error bars denote ±1 SD across five RF training folds. Inset pie charts show the four variables with the largest absolute Shapley values, with the remaining four variables grouped as "Others." Slice percentages are calculated as $100 \times |\varphi_i|/\Sigma_j|\varphi_j|$ and therefore represent relative contribution magnitudes, irrespective of sign. Red hatching identifies negative contributions displayed as individual slices. "Others" combines the absolute magnitudes of the remaining modeled contributions, which may include both positive and negative values; it does not represent unexplained model error. Percentages are rounded and may not sum to 100%. The boxed value reports the signed sum of Shapley contributions, $\Sigma_i\varphi_i$, equal to the modeled greenness-area trend under the full scenario minus that under the reference scenario in which all eight climate variables are detrended. See Materials and Methods for the random-forest models, detrending procedure, and Shapley calculations.

Supplementary Files

This is a list of supplementary files associated with this preprint. Click to download.

- DataS3.xlsx
- DataS4.csv
- SupplementarymaterialsSatelliteobservedgreennessexpansionacrossAntarctica.docx
- DataS2.xlsx
- DataS1.csv